ACS APPLIED MATERIALS & INTERFACES

RESEARCH ARTICLE

www.acsami.org

Hydrothermally Synthesized Titanate Nanostructures: Impact of Heat Treatment on Particle Characteristics and Photocatalytic Properties

Kunlanan Kiatkittipong, Jason Scott, and Rose Amal*

ARC Centre of Excellence for Functional Nanomaterials, School of Chemical Engineering, The University of New South Wales, Sydney, NSW 2052, Australia

ABSTRACT: The role titanate particle structure plays in governing its characteristics upon calcining and their ensuing influence on photocatalytic performance was investigated. Titanate nanotubes and nanoribbons were prepared by hydrothermal treatment of Aeroxide P25 and then calcined at temperatures in the range 200 - 800 °C. Heat treatment directly transformed the nanotubes to anatase while nanoribbon transformation to anatase occurred via a TiO_2(B) intermediate phase. The nanoribbon structure also provided an increased resistance to sintering, allowing for retention of the original {010} facet of the titanate nanosheets up to 800 °C. The changing material properties with calcining were found to influence the capacity of the particles to photodegrade oxalic acid and methanol. The nanotubes provided an optimum photoactivity following calcination at 500 °C with this point representing a transition between the relative dominance of crystal phase and surface area on performance. The comparatively smaller initial surface area of the nanoribbons consigned this characteristic to a secondary role in influencing photoactivity with the changes to crystal phase dominating the continually improving performance with calcination up to 800 °C. The structural stability imparted by the nanoribbon architecture during calcination, in particular its retention of the {010} facet at temperatures >700 °C, advanced its photocatalytic performance compared with the nanotubes. This was especially the case for methanol photooxidation whose primary degradation mechanism relies on hydroxyl radical attack and was facilitated by the {010} facet. The effect was not as pronounced for oxalic acid due to its higher adsorption on TiO_2 and therefore greater susceptibility to oxidation by photogenerated holes. This study demonstrates that, apart from modulating sintering effects and changes to crystal phase, the titanate nanostructure influences particle crystallography which can be beneficial for photocatalytic performance.

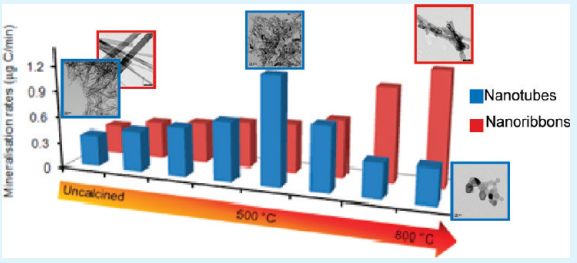

KEYWORDS: titanate, nanotube, nanoribbon, calcination, organic adsorption, photocatalytic activity

1. INTRODUCTION

With awareness of the increasing levels of pollutants in air and water, photocatalytic oxidation of organic compounds, especially in environmental-related applications, has been intensively studied.[1−4] Among the many photocatalyst candidates, titanium dioxide (TiO_2) is a common choice due not only to its photocatalytic attributes but also its low cost and benign nature.[5] In addition, Ti−O-based nanostructures possessing various architectures can be readily tailored and have been proposed to impart advantageous characteristics depending on the particular morphology. For example, Yu et al. observed the photocatalytic activity of a nanofibrous TiO_2 structure exceeded that of Degussa P25 for vapor phase photocatalytic oxidation of acetone in air.[6] Ti−O nanostructures with a high aspect ratio may invoke a high charge transfer rate[7] and decreased electron hole recombination[8] compared with their bulk counterparts.

The simple preparation of titanium oxide nanotubes was first reported by Kasuga et al. using hydrothermal synthesis by reacting TiO_2 particles with concentrated NaOH followed by acid washing.[9] The synthesis conditions could be adjusted to fabricate alternate titanate structures, including nanosheets, nanorods/nanowires and nanoribbons/nanobelts.[8,10−14] On the basis of their high surface area, titanate nanostructures have been proposed as good candidates for organic photomineralization.[15] Nakahira et al. reported that as-prepared titanate nanotubes showed a high photocatalytic activity for formaldehyde decomposition in the aqueous phase.[16] Moreover, titanate nanofibers were found by Zhu et al. to be active for synthetic dye degradation under UV light.[17] On the other hand, Yu et al. and Inagaki et al. observed no photocatalytic activity for acetone degradation in the gas phase over as-prepared titanate nanowires and nanotubes.[18−20] Similarly, hydrothermally synthesized titanate was found to be inactive for amaranth dye and azo dyes.[21,22] The reduced performance was attributed to titanate being an inactive phase and possessing low crystallinity,[20,21] although the model organic may have also been a contributing factor[23]

Calcination may be used to improve the photocatalytic properties of a material by promoting its crystallinity, converting it to a more active crystal phase or reducing surface defects. Calcining titanate nanostructures invariably leads to the formation of

Received: July 1, 2011
Accepted: September 22, 2011
Published: September 22, 2011

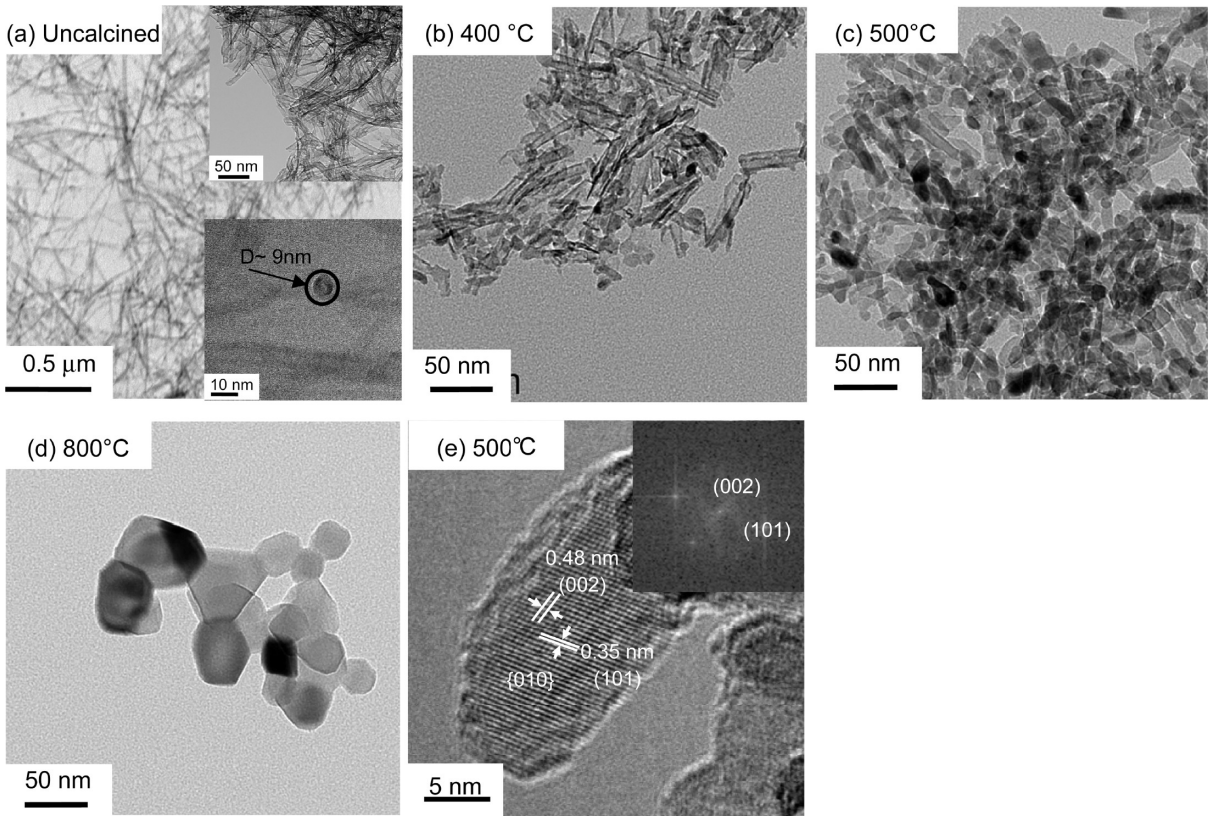

Figure 1. (a) TEM image of uncalcined nanotubes; (b–d) high-resolution TEM images of nanotubes calcined at 400, 500, 800 °C, respectively; (e) high-resolution TEM image and corresponding fast Fourier transformation (FFT) of particle obtained from nanotubes calcined at 500 °C.

crystalline TiO_2 with the phase attained being governed by the calcination temperature and potentially the original structure. For instance, titanate nanotubes have been reported to transform to anatase at temperatures higher than 200 °C,[10,24−26] while calcining titanate nanowires/fibers/ribbons at 200−400 °C has been observed to form TiO_2(B) as an intermediate phase after which conversion to anatase occurred at higher (>400 °C) temperature.[19,27−31] TiO_2(B) was also observed by Armstrong et al. during calcination of their titanate nanotubes.[32] Phase transformation invoked by calcination has been shown to improve photoactivity as detailed in a number of studies.[19,22,26,28,33,34]

The crystal facets of anatase can exhibit different photocatalytic activities as detailed by Pan et al (2011).[35] In particular the more energetic but less prevalent {010} facet has been described as the most photoactive of the facets ({101}, {001} and {010}) present on the surface of a generic anatase crystallite. Recently, the dominant {010} facet in anatase nanorods was reported to significantly enhance the photocatalytic conversion of CO_2 into methane when compared to TiO_2 P25.[36]

While studies have demonstrated calcining titanate nanostructures incites its transformation to various TiO_2 crystal phases and can improve photoactivity, no direct assessment of the role the structure plays in the phase transformation process nor the resulting photoactivity has been attempted. Additionally, the impact of calcination on titanate particle crystallography and its potential relationship with photoactivity has not been considered. This study probes the influence of nanostructure on these characteristics, comparing titanate nanotube and nanoribbon phase transformation during calcination and their subsequent photodegradation of two organic compounds, oxalic acid (a strongly adsorbed organic compound) and methanol (a weakly adsorbed organic compound).

2. EXPERIMENTAL SECTION

2.1. Reagents. Aeroxide P25 titanium dioxide (80% anatase, 20% rutile (Sigma-Aldrich)), sodium hydroxide (Ajax Finechem), hydrochloric acid (32 vol%, Ajax Finechem), perchloric acid, oxalic acid and methanol were used without further purification.

2.2. Nanotube and Nanoribbon Synthesis. Titanate nanostructures were synthesized using a hydrothermal procedure. Initially, 0.5 g of Aeroxide P25 TiO_2 and 20 mL of 10 M NaOH were stirred for 1.5 h in a plastic bottle. The slurry was transferred to a Teflon-lined autoclave, sealed and heat treated in an oven at (i) 150 °C for 72 h to produce the nanotubes or (ii) 200 °C for 24 h to produce the nanoribbons. The resulting suspension was washed first with 0.1 M HCl and then with water until the pH value of the wash solution reached approximately 6. After centrifuging and drying at 80 °C for 72 h, the products were calcined at temperatures between 200 and 800 °C. During calcination the temperature was ramped at 5 °C min^{-1} with the samples held at the desired temperature for 2 h.

2.4. Characterization. Crystal and structural characteristics of the products were investigated by powder X-ray diffraction (XRD) performed on a Philips X'pert multipurpose X-ray diffraction system with monochromatized $Cu_{k\alpha}$ radiation (χ = 1.5418 Å). Sample morphology was assessed by transmission electron microscopy (TEM, JEOL 1400 and Phillips CM200 including HRTEM). The surface area and pore size distribution was determined by N_2 adsorption (BET method, Micromeritics Tristar). Optical properties of the samples were characterized by UV−visible spectroscopy (Cary 300).

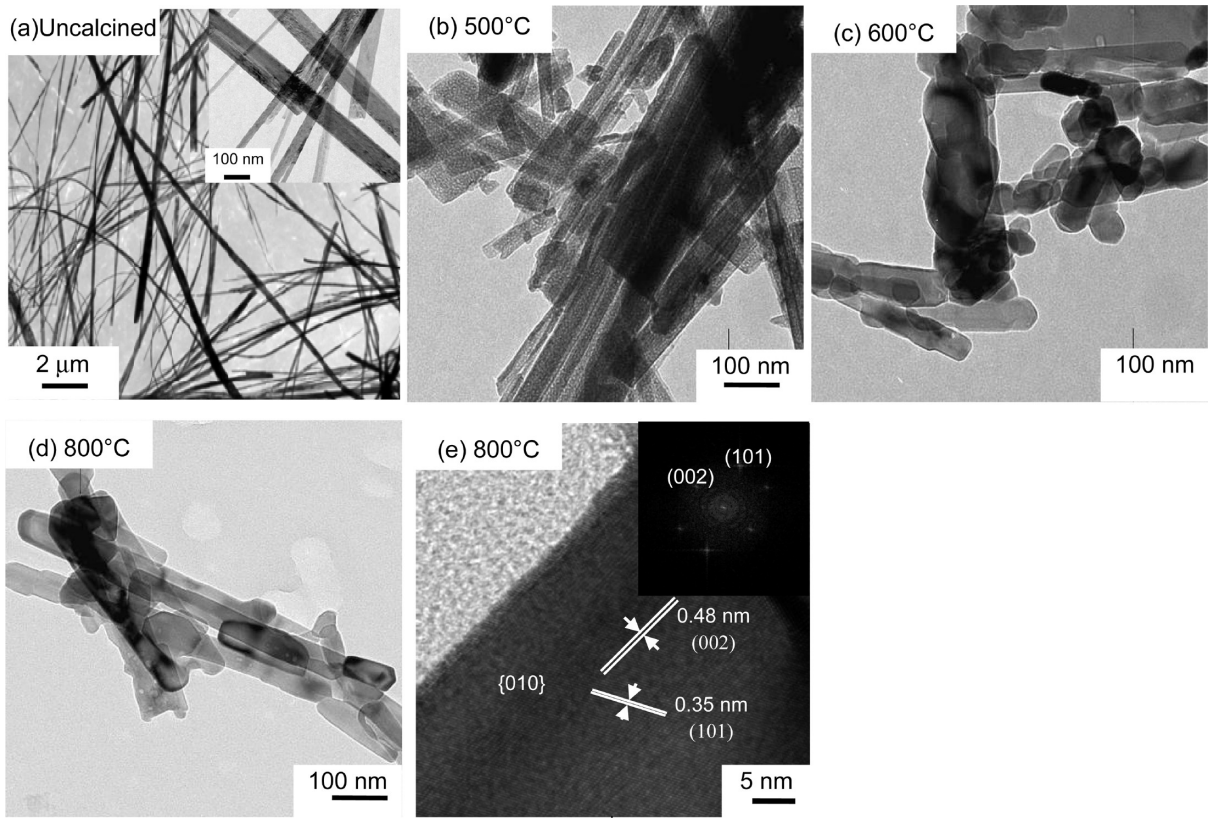

Figure 2. (a) TEM images of uncalcined nanoribbons; (b−d) high-resolution TEM images of nanoribbons calcined at 500, 600, 800 °C, respectively; (e) high-resolution TEM image and corresponding fast Fourier transformation (FFT) of particle obtained from nanoribbons calcined at 800 °C.

2.5. Photocatalytic Activity. Photocatalytic activity was assessed by studying the mineralization of oxalic acid and methanol in acidified water. The initial organic concentration was 1000 μg (as carbon) and a 0.5 g/L catalyst loading was employed. In a typical experiment, 60 mL of the photocatalyst suspension was added to a glass spiral reactor and 1 M perchloric acid used to adjust the pH to 3 ± 0.05. Prior to organic addition, the suspension was illuminated using a UV−C lamp (λ_{max} = 254 nm) for 40 min to remove impurities from the photocatalyst surface. The suspension was then air equilibrated for 20 min after which the organic compound was injected and the system allowed to circulate for a further 20 min. The lamp was turned on and photocatalytic degradation monitored by the rate of CO_2 generation in the system. The relative activity of samples calcined at different temperatures was evaluated by comparing the half-life mineralization rate for CO_2 generation.

3. RESULTS AND DISCUSSION

The TEM images in Figure 1a and 2a reveal morphologies of the titanate nanostructures hydrothermally synthesized at 150 °C for 72 h and 200 °C for 24 h are nanotubes and nanoribbons, respectively. The nanotubes have an outer diameter of approximately 9 nm and length in the order of micrometers while the nanoribbons have a width of 10−100 nm and a length also in the order of micrometers. This nanotube diameter falls in the range described by Yu et al. (7−15 nm)[18] and Qamar et al. (6−10 nm)[21] and the particles are of similar length. The nanoribbon diameter range is broader than that reported by Jitputti et al. (20−40 nm),[37] although they synthesized their particles at 150 °C for 72 h. The formation of nanowires by Jitputti et al., despite using conditions expected to produce nanotubes, may have arisen from the particular acid washing conditions used in their work. The role of hydrothermal temperature on the final particle morphology has been previously described by Bavykin et al.[38] During the initial stages of the hydrothermal process crystal titanate sheets are formed. At milder temperatures (i.e., 150 °C), the kinetics of layer formation of these titanate sheets are slow enough to allow for their rolling up leading to nanotube formation. At higher temperatures, titanate sheet growth and layering is rapid, in turn favoring formation of 'thicker' structures, which then suppress the structural forces responsible for any roll-up effect. Consequently, the flat nanoribbon structure is obtained.

The sequence of TEM images in Figure 1b−d illustrates the influence of calcination on titanate nanotube morphology. As the calcination temperature was increased over the range 200 to 400 °C the nanotubes became increasingly fragmented and, as seen in Figure 1b, by 400 °C some nanotubes had collapsed to produce nanoparticles. Calcining at 500 °C resulted in complete structural collapse of the nanotubes with the particles becoming a mixture of elongated and irregularly shaped morphologies. Complete collapse of the nanotube architecture by 500 °C is consistent with the findings of others.[18,22,39,40] Xiao et al. observed structural collapse of their nanotubes at 500−600 °C; however, they used a variation in synthesis conditions (hydrothermal treatment at 140 °C for 12 h), which produced $H_2Ti_4O_9 \cdot H_2O$ as opposed to the trititanate ($H_2Ti_3O_7$) structure reported by the preceding studies.[41] By 800 °C considerable sintering and agglomeration had occurred whereby the particles had increased in size to between 25 and 70 nm. A HRTEM image for the particles calcined at 500 °C is provided Figure 1e. It depicts

Table 1. Structural and Optical Properties of Uncalcined and Calcined Nanotubes and Nanoribbons

structure	calcination temperature (°C)	surface area (m^2/g)	crystalite size of anatase[a] (nm)	band gap energy (eV)
nanotube	uncalcined	313		3.56
	200	280	8.20	3.52
	300	255	9.21	3.50
	400	225	9.95	3.50
	500	106	13.76	3.48
	600	52	18.93	3.48
	700	23	30.78	3.30
	800	5	40.73	3.30
nanoribbon	uncalcined	26		3.56
	200	24		3.52
	300	22		3.50
	400	21		3.50
	500	19	11.29	3.50
	600	15	20.00	3.48
	700	6	47.90	3.29
	800	5	47.90	3.29

[a] Empty entries indicate the absence of an anatase phase.

a well-defined internal crystal lattice encompassed by a less-defined outer layer which was similarly observed by Yu et al.[18] The interplanar spacing of the particle calcined at 500 °C, corresponding to the (101) crystal plane of anatase, is 0.35 nm which also agrees well with the findings by Yu et al.[18] for titanate nanotubes calcined at 500 °C. The calculated interplanar spacing of the (002) plane is 0.48 nm as also shown in Figure 1e. In addition, the particle calcined at 500 °C possessed a distinct crystal structure pertaining to a dominant {010} exposed facet. However, a dominant crystal facet could not be identified following particle transformation from elongated morphologies to irregular shapes at temperatures higher than 700 °C.

TEM images in Figure 2b–d depict the impact of calcining the titanate nanoribbons on their morphology. Figure 2b shows the nanoribon structure is preserved at 500 °C, although some fragmentation had occurred. Calcination at 600 °C invoked a distinct change in particle morphology as, although some particles retained an elongated structure, other more spherical particles were also present. Particle morphology after calcining at 800 °C was similar to that for the 600 °C temperature with a mixture of elongated and irregularly shaped particles. Jitputti et al. observed structural stability in their nanowires at calcination temperatures up to and beyond 800 °C.[37]

Figure 2e indicates that the dominate crystal facet for titanate nanoribbons calcined at 800 °C is {010}, which was similar to that observed for the nanotubes calcined at 500 °C. It is interesting to note that nanoribbons can retain their facet at higher temperature, which may be attributed to the thicker nanosheet layers of the nanoribbon particles. That is, the greater number of stacked nanosheets acts to stabilize the crystal structure against rearrangement at higher calcination temperatures.

Transformation of the nanostructures with calcination temperature is reflected by the change in specific surface area as detailed in Table 1. The titanate nanotubes have an initial specific surface area of 313 m^2/g which is slightly lower than the values reported by Yu et al.[18] and Qamar et al.[21] (~350 m^2/g). The specific surface area decreases to 225 m^2/g when the sample was

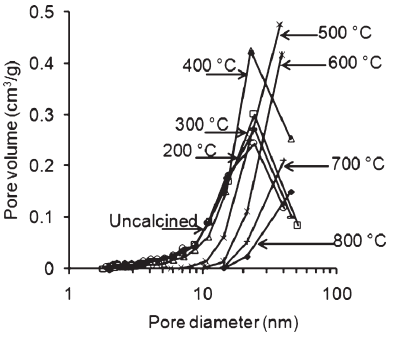

Figure 3. Pore size distribution of uncalcined nanotubes and nanotubes calcined at 200–800 °C.

calcined at 400 °C. Calcination at 500 °C further decreases the specific surface area (106 m^2/g), which corresponds to the complete collapse of the nanotube structure as was illustrated in Figure 1. The ruinous loss of tube structure at 500 °C (and above) is reflected by the loss of pore volume for pores below 8 nm in diameter (Figure 3). This is again comparable with the work by Yu et al.[18] who reported a complete loss of tube pores <10 nm in diameter following nanotube calcination at 500 °C. Increases in calcination temperature above 500 °C promote a further decrease in specific surface area as particle sintering and agglomeration occurs agreeing with the findings of others.[18,21,24]

The titanate nanoribbons possessed a comparatively low initial surface area (26 m^2/g) which decreased to approximately 19 and 15 m^2/g for samples calcined at 500 and 600 °C, respectively. At 700 °C and above the structure had crumbled and the specific surface area reduced to 5 m^2/g. The drop in the specific surface area between 500 and 700 °C corresponded to the change in particle morphology depicted in Figure 2. Jitputti et al. reported a higher initial surface area of their titanate nanowires (150 m^2/g), which likely arose from the slimmer structure their particles possessed[37]. They also observed a continual decrease in surface area with increasing calcination temperature, reaching ~13 m^2/g by 800 °C.

The XRD patterns in Figure 4 demonstrate the phase transformation resulting from nanotube calcination. The uncalcined nanotube profile in Figure 4a confirms the presence of hydrogen titanate ($H_2Ti_3O_7$), with the reflection peak at $2\theta \approx 9°$ corresponding to interlayer spacing between the titanate sheets. Calcining at 200 °C leads to disappearance of the peak at $2\theta \approx 9°$ due to dehydration of moisture located between titanate layers, and the appearance of small peaks at 53°, 55° and 63° corresponding to the anatase phase of TiO_2. Similar findings were reported by Vijayan et al. (2010)[31] and others[21,41] whereby anatase was present in the sample by 300 °C. Increasing the calcination temperature to 400 °C promoted the continued formation of anatase (Figure 4b–h) as well as a minor growth in the crystal size (Table 1). Calcining at 500 °C leads to a comparatively larger crystal size which corresponds to the collapse of the nanotube architecture (Figure 1). Increasing the calcination temperature beyond 500 °C promotes further growth in crystal size and conversion of the entire structure to anatase. No evidence of rutile formation at calcination temperatures up to 800 °C was found, which agrees with Tsai and Teng[24] for titanate nanotubes hydrothermally treated at temperatures greater than 130 °C. However, rutile has been reported to form in nanotubes at temperatures lower than 800 °C by other research groups.[18,41–43]

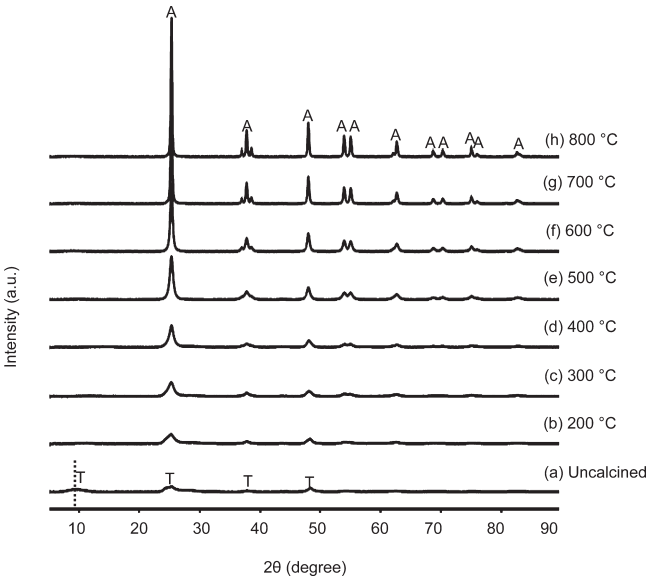

Figure 4. XRD patterns of uncalcined nanotubes and nanotubes calcined from 200 to 800 °C. T = titanate phase; A = anatase phase.

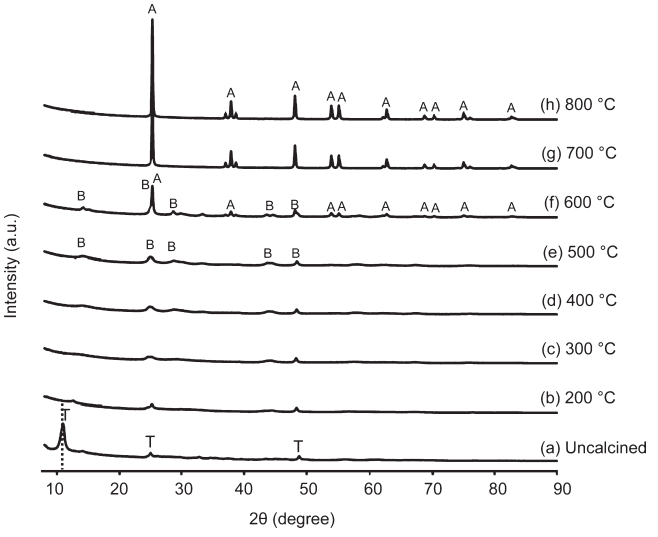

Figure 5. XRD of uncalcined nanoribbons and nanoribbons calcined from 200 to 800 °C. T = titanate phase; B = TiO_2(B) phase; A = anatase phase.

XRD patterns for the uncalcined and calcined nanoribbons are provided in Figure 5. The spectra for the uncalcined nanoribbons can be indexed to hydrogen titanate ($H_2Ti_3O_7$) with the peak at $2\theta \approx 11°$ corresponding to interlayer spacing between the titanate sheets. The shift in this peaks position, compared with the titanate nanotubes, derives from bending of the multilayered sheets in the nanotube configuration.[44] Calcining from 200 to 500 °C sees a significant loss in intensity of the $2\theta \approx 11°$ peak as well as its broadening and shift to a higher value ($2\theta \approx 14°$). This stems from structural dehydration of the titanate nanoribbons and their ensuing conversion to the monoclinic TiO_2(B). TiO_2-(B) formation is confirmed by the onset and gradual intensifying of peaks at $2\theta \approx 28$ and 47° as the calcination temperature is increased. At 500 °C, the nanoribbons comprise TiO_2(B) mixed with ~24% anatase (calculated using Scherrer's equation), with the anatase proportion increasing to 74% by 600 °C. Bulk conversion from TiO_2(B) to anatase across this temperature region corresponds with nanoribbon fragmentation and morphology change as evident in Figure 2. At calcination temperatures of 700 °C and beyond the structure is completely converted to anatase. An analogous nanowire phase transition at the same calcination temperatures has been described by Jitputti et al.[37] Nanoribbon conversion to anatase and its crystal growth are quantified in Table 1.

A schematic depicting structural and phase transformations of the titanate nanotubes and nanoribbons into anatase with increasing calcination temperature is provided in Figure 6. On comparison, distinct differences are evident in the event lines for the two structures.

Transformation of the nanotube from the titanate to the anatase phase does not occur via an intermediate phase (TiO_2(B)) as is the case for the nanoribbons. Furthermore, structural collapse occurs at a lower temperature for the nanotubes. Variations in these transformation events originate from the different degrees of nanosheet stacking and the ensuing structural stability a greater number of sheets provides. The nanoribbon system comprises multilayered titanate sheets which appear to provide a stronger "bulk" structure, enabling greater resistance to mobility of the titania octahedra at elevated temperatures. The titanate nanotubes, on the other hand, contain a low sheet stacking density which reduces its opposition to sintering during calcination. This effect manifests itself not only in the decreased resistance of nanotubes to sintering but also in the prolonged presence of the metastable TiO_2(B) phase during nanoribbon calcination as well as retention of the {010}crystal facet at temperatures up to 800 °C. It is conceivable TiO_2(B) is formed during nanotube transformation from titanate to anatase; however, its presence may be short-lived (occurring below 200 °C) because of the weaker nature of this configuration.

Calcination was observed to influence optical properties of both nanostructure types as depicted in Figure 7. The absorption edge of the uncalcined nanotubes moved from ~355 nm to ~363 nm (Figure 7a) on calcining at 200 °C as a consequence of the structural dehydration. Calcining at 300 °C invoked a red shift in the absorption edge to ~365 nm where it resided up to a temperature of 400 °C. A further increase in temperature to 500 °C promoted an additional red shift in the absorption edge to 367 nm which then again shifted to approximately 373 nm as the temperature increased to 700 °C. The shifts in absorption edge are reflected in the band gap values provided in Table 1. The changes in band gap energy likely derive from the transformations in crystal phase and, to a lesser extent, particle morphology. Similar shifts in band gap energy with calcination have been reported by others.[19,22,39] The nanoribbons (Figure 7b) exhibited similar absorption onsets and shifts with calcination temperature to that experienced by the nanotubes with the exception that the shift to 367 nm is observed to start at 600 °C. This delay is anticipated to derive from the different rates of change in crystal phase of the nanostructures as detailed earlier.

The influence of calcination temperature and change in particle characteristics of the two nanostructures on the photomineralization rates of oxalic acid and methanol are illustrated in Figures 8 and 9, respectively. The organics were selected based on their extensive (oxalic acid)[45−47] and limited (methanol)[45,48] adsorption on TiO_2, reflecting direct

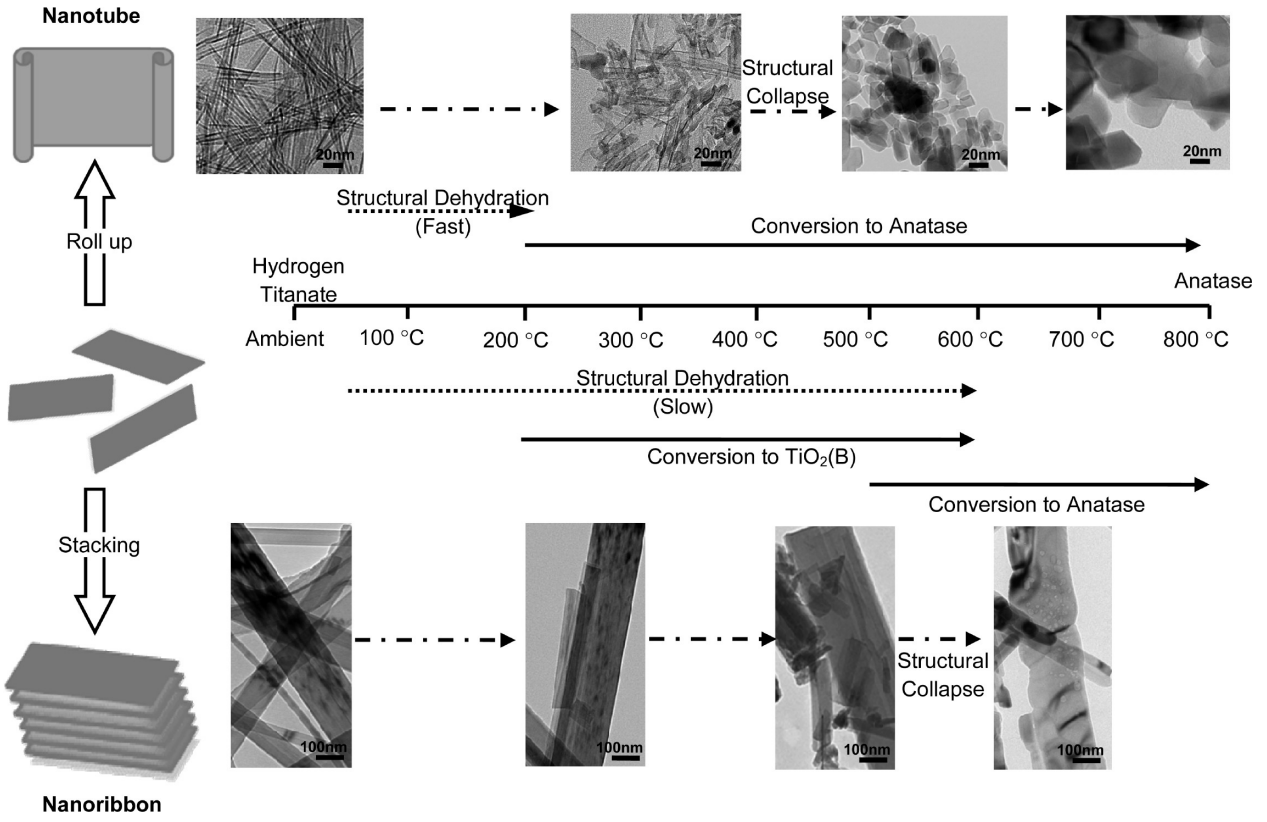

Figure 6. Schematic diagram showing phase structural transformations of nanotubes and nanoribbons with calcining up to 800 °C.

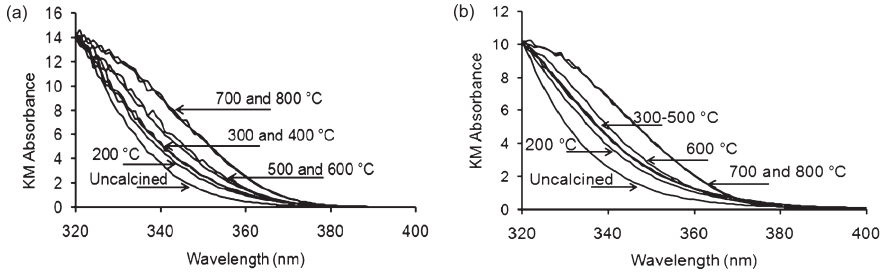

Figure 7. UV−visible spectra of: (a) uncalcined nanotubes and nanotubes calcined at 200−800 °C; (b) uncalcined nanoribbons and nanoribbons calcined at 200−800 °C.

hole photooxidation and indirect hydroxyl radical photooxidation mechanisms, respectively.

Figure 8 reveals distinct differences between the oxalic acid photomineralization rates with calcination temperature for each nanostructure. Photomineralization by the nanotubes is characterized by a maximum rate at calcination temperatures between 400 and 500 °C, whereas the nanoribbons exhibit a continual increase in rate over the entire calcination range. Nanotube photoactivity is observed to increase with calcination temperature up to 400 °C, despite an approximately 30% decrease in surface area (Table 1). The improvement can be explained by the initial structural dehydration and consequent gradual increase in anatase content, highlighting the dominant impact of crystal phase over this region. The calcination zone of 400 to 500 °C represents a transition between the relative dominance of crystal phase and surface area as, beyond 500 °C, the photoactivity decreases irrespective of the improving anatase crystallinity and loss of titanate component. Other studies have reported a similar optimum photocatalytic performance of titanate nanotubes calcined at between 400 and 500 °C for a range of organics in both the aqueous (methyl orange,[41] amaranth[21]) and gas (acetone,[18] propylene[40]) phases. The uncalcined titanate nanostructures exhibited photoactivity in this instance which was similarly observed in some studies[49] but not so in others.[18,21] Variations in the photocatalytic performance of the uncalcined nanotubes may derive from particle differences but can equally originate from the choice of organic compounds. Ryu and Choi demonstrated the different photocatalytic performance of a selection of commercial TiO_2 samples was linked to the class of organic (e.g., carboxylic acid, aromatic, dye) being photodegraded, and is a potential explanation in this instance.[23]

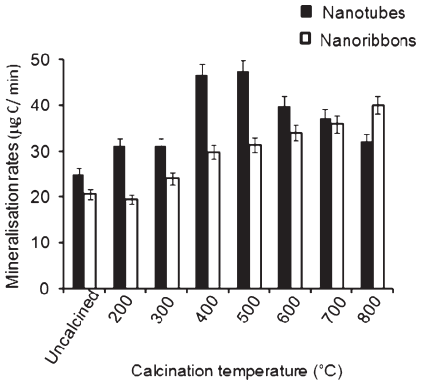

Figure 8. Fifty percent photocatalytic mineralization rate (R_{50}) of oxalic acid (as 1000 μg C) in the presence of 0.5 g/L uncalcined nanotubes/nanoribbons and nanotubes/nanoribbons calcined at temperatures from 200 to 800 °C.

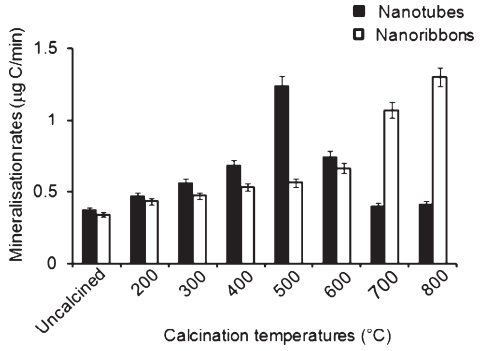

Figure 9. (a) Fifty percent photocatalytic mineralization rate (R_{50}) of methanol (as 1000 μg C) in the presence of 0.5 g/L uncalcined nanotubes/nanoribbons and nanotubes/nanoribbons calcined at temperatures from 200 to 800 °C.

In contrast to the nanotubes, the comparatively low initial surface area of the nanoribbons suppresses the potential for this trait to have any influence on photoactivity. Instead, nanoribbon photoactivity appears to be governed by the change in crystal phase with calcination temperature, increasing in the order $H_2Ti_3O_7$ < TiO_2(B) < mixed TiO_2(B)/anatase < anatase. A similar relationship has been observed for phenol photodegradation[28,50] and photocatalytic hydrogen evolution using methanol.[37] The higher activity of the pure anatase phase in relation to the mixed anatase/TiO_2(B) phase however disagrees with findings by Yang et al.[51] and Zhou et al.[52] who reported an improvement in photocatalytic performance by their mixed phase systems. Yang et al's particles comprised a fibril TiO_2(B) core surrounded by an anatase shell while Zhou et al's particles comprised TiO_2(B) nanobelts loaded with anatase nanoparticles. In both instances the anatase component was loaded onto a titanate structure by acid treatment followed by calcination to convert titanate to TiO_2(B). The photoactivity improvement invoked by these heterostructures (which was not observed in our particles) was ascribed to their ability to mediate photogenerated hole migration across the phase interface into TiO_2(B) and reduce recombination. This effect may be enhanced by: (1) clarity of the definition between phase boundaries and; (2) the size and continuity of the anatase/TiO_2(B) features in the heterostructures.

The phase mixture of the nanoribbons in this study is anticipated to be more homogeneous than those reported above with an initial low level of small anatase inclusions in the TiO_2(B) bulk, gradually increasing until the inverse circumstance (i.e., small TiO_2(B) inclusions in the anatase bulk) occurs. Consequently, the potential for hole migration from anatase to TiO_2(B) may be diminished by the more homogeneous structure.

The influence of calcination temperature on methanol (limited adsorption on TiO_2) photomineralization rates by both nanostructures was similar to that observed for oxalic acid (extensive adsorption on TiO_2). That is, a maximum photomineralization rate was seen for samples heat treated at 500 °C for the nanotubes, whereas the photomineralization rate continually increased for the nanoribbons.

However, differences between the mineralization findings for the two organics are also apparent. First, the R_{50} values for methanol oxidation are a factor of 40 (or greater) lower than the values for oxalic acid oxidation. The consistent difference in these values likely originates from the mechanisms dominating their photodegradation, which may in turn be attributed to their degree of adsorption. Oxalic acid is extensively adsorbed on TiO_2,[53] meaning its oxidation by photogenerated holes can play a substantial role. Methanol is poorly adsorbed on TiO_2[53] meaning it is more reliant on oxidation by hydroxyl radicals (generated from the oxidation of water and surface hydroxyl groups) in solution. It is apparent from the overall mineralization rates oxidation by hydroxyl radicals is considerably more arduous than when holes also participate in the process.

Second, both organic mineralization rates for the nanoribbons calcined at 800 °C are greater than the corresponding nanotube rates. The R_{50} values for the two nanostructures calcined at 800 °C indicate the nanoribbons are more proficient at mineralizing both organics (~20% for oxalic acid, ~80% for methanol) despite the two materials exhibiting similar physical characteristics (Table 1). In the case of methanol this is also apparent for the structures calcined at 700 °C, even with the nanotubes having a four times greater advantage in terms of surface area. This peculiarity may arise from the higher prevalence of the {010} facet on the nanoribbons calcined at 700 °C and above (Figure 2e) compared with the nanotubes when calcined at the same temperatures (Figure 1d). The {010} facet has been reported by Pan et al.[35] to be more photoactive than the {101} and {001} facet of TiO_2, particularly for hydroxyl radical generation, supporting the findings of this work. They attributed the higher photoactivity of the {010} facet to a combination of its more favorable surface atomic and surface electronic structures, which promote the efficient photoreduction reactions and photooxidation reactions, simultaneously. The impact of the {010} facet is particularly noticeable for methanol given its photooxidation mechanism is primarily mediated by hydroxyl radical attack.

4. CONCLUSIONS

Titanate nanostructure morphology was found to influence structural stability and particle characteristics when subject to calcination. The multiple stacked titanate sheets of the nanoribbons provided greater resistance to change with increasing calcination temperature compared to the rolled titanate sheets of the nanotubes. For the nanoribbons, this manifested itself as the formation of an intermediate TiO_2(B) phase during

conversion to anatase and greater retention of the original {010} facet of the titanate nanosheets. The nanotubes on the other hand were directly converted to anatase with no observed prevalence for the {010} facet, particularly at elevated temperatures, and were subject to a considerable loss in surface area.

The extent to which these changes influenced the materials photocatalytic performance was governed by both the particle characteristics and the targeted organic or, more critically, its preferred photodegradation mechanism. In the case of the nanotubes, the optimum photoactivity occurred for samples calcined at ~500 °C with this temperature reflecting the transition in dominance between crystal phase and surface area. Photoactivity of the nanoribbons continually increased with increasing calcination temperature, due primarily to the change in crystal phase from titanate to TiO_2(B) to anatase. However, the structural stability invoked by the nanoribbons and the consequent retention of the {010} facet at elevated calcination temperatures (>700 °C) proved beneficial for its photoactivity. This was especially the case for methanol photodegradation due to its reliance on hydroxyl radical attack for its oxidation.

This study ascertained that titanate particle architecture can have a significant impact on its characteristics when subject to calcination. This can be in the form of, for instance, resistance to sintering, phase transformation, and as demonstrated here, crystallographic retention. The extent to which these characteristics are either altered or retained then influences photocatalytic performance.

AUTHOR INFORMATION

Corresponding Author
*E-mail: r.amal@unsw.edu.au.

ACKNOWLEDGMENT

This work was financially supported by the ARC Centre of Excellence for Functional Nanomaterials. The authors thank Dr. Aaron Dodd for his assistance with the HRTEM and Dr. Yu Wang for his support with XRD measurements.

REFERENCES

(1) Hoffmann, M. R.; Martin, S. T.; Choi, W.; Bahnemann, D. W. *Chem. Rev.* **1995**, *95*, 69–96.
(2) Legrini, O.; Oliveros, E.; Braun, A. M. *Chem. Rev.* **1993**, *93*, 671–698.
(3) Denny, F.; Permana, E.; Scott, J.; Wang, J.; Pui, D. Y. H.; Amal, R. *Environ. Sci. Technol.* **2010**, *44*, 5558–5563.
(4) Irawaty, W.; Friedmann, D.; Scott, J.; Amal, R. *J. Mol. Catal. A: Chem.* **2011**, *335*, 151–157.
(5) Hashimoto, K.; Irie, H.; Fujishima, A. *Jpn. J. Appl. Phys., Part 1* **2005**, *44*, 8269–8285.
(6) Yu, J.; Yu, H.; Cheng, B.; Zhao, X.; Zhang, Q. *J. Photochem. Photobiol., A* **2006**, *182*, 121–127.
(7) Chen, X.; Mao, S. S. *Chem. Rev.* **2007**, *107*, 2891–2959.
(8) Zhou, W.; Liu, H.; Wang, J.; Liu, D.; Du, G.; Cui *J. ACS Appl. Mater. Interfaces* **2010**, *2*, 2385–2392.
(9) Kasuga, T.; Hiramatsu, M.; Hoson, A.; Sekino, T.; Niihara, K. *Langmuir* **1998**, *14*, 3160–3163.
(10) Sun, X.; Li, Y. *Chem.—Eur. J.* **2003**, *9*, 2229–2238.
(11) Morgan, D. L.; Zhu, H. Y.; Forst, R. L.; Waclawik, E. R. *Chem. Mater.* **2008**, *20*, 3800–3802.
(12) Yoshida, R.; Suzuki, Y.; Yoshikawa, S. *J. Solid State Chem.* **2005**, *178*, 2179–2185.
(13) Kiatkittipong, K.; Ye, C.; Scott, J.; Amal, R. *Cryst. Growth Des.* **2010**, *10*, 3618–3625.
(14) Wang, C.; Yin, L.; Zhang, L.; Liu, N.; Lun, N.; Qi, Y. *ACS Appl. Mater. Interfaces* **2010**, *2*, 3373–3377.
(15) Guo, G. S.; He, C. N.; Wang, Z. H.; Gu, F. B.; Han, D. M. *Talanta* **2007**, *72*, 1687–1692.
(16) Nakahira, A.; Kato, W.; Tamai, M.; Isshiki, T.; Nishio, K.; Aritani, H. *J. Mater. Sci.* **2004**, *39*, 4239–4245.
(17) Zhu, H.; Gao, X.; Lan, Y.; Song, D.; Xi, Y.; Zhao, J. *J. Am. Chem. Soc.* **2004**, *126*, 8380–8381.
(18) Yu, J.; Yu, H.; Cheng, B.; Trapalis, C. *J. Mol. Catal. A: Chem.* **2006**, *249*, 135–142.
(19) Yu, H.; Yu, J.; Cheng, B. *Chemosphere* **2007**, *66*, 2050–2057.
(20) Inagaki, M.; Kondo, N.; Nonaka, R.; Ito, E.; Toyoda, M.; Sogabe, K.; Tsumura, T. *J. Hazard. Mater.* **2009**, *161*, 1514–1521.
(21) Qamar, M.; Yoon, C. R.; Oh, H. J.; Lee, N. H.; Park, K.; Kim, D. H.; Lee, K. S.; Lee, W. J.; Kim, S. *J. Catal. Today* **2008**, *131*, 3–14.
(22) Mozia, S. *Catal. Today* **2010**, *156*, 198–207.
(23) Ryu, J.; Choi, W. *Environ. Sci. Technol.* **2008**, *42*, 294–300.
(24) Tsai, C. C.; Teng, H. *Chem. Mater.* **2004**, *16*, 4352–4358.
(25) Suetake, J.; Nosaka, A. Y.; Hodouchi, K.; Matsubara, H.; Nosaka, Y. *J. Phys. Chem. C* **2008**, *112*, 18474–18482.
(26) Sreekantan, S.; Wei, L. C. *J. Alloys Compd.* **2010**, *490*, 436–442.
(27) Pavasupree, S.; Suzuki, Y.; Yoshikawa, S.; Kawahata, R. *J. Solid State Chem.* **2005**, *178*, 3110–3116.
(28) Mu, R.; Xu, Z.; Li, L.; Shao, Y.; Wan, H.; Zheng, S. *J. Hazard. Mater.* **2010**, *176*, 495–502.
(29) Lin, C. H.; Chao, J. H.; Liu, C. H.; Chang, J. C.; Wang, F. C. *Langmuir* **2008**, *24*, 9907–9915.
(30) Armstrong, A. R.; Armstrong, G.; Canales, J.; Bruce, P. G. *Angew. Chem., Int. Ed.* **2004**, *43*, 2286–2288.
(31) Vijayan, B.; Dimitrijevic, N. M.; Rajh, T.; Gray, K. *J. Phys. Chem. C* **2010**, *114*, 12994–13002.
(32) Armstrong, G.; Armstrong, A. R.; Canales, J.; Bruce, P. G. *Chem. Commun.* **2005**, 2454–2456.
(33) An, H.; Zhu, B.; Li, J.; Zhou, J.; Wang, S.; Zhang, S.; Wu, S.; Huang, W. *J. Phys. Chem. C* **2008**, *112*, 18772–18775.
(34) Xiong, L.; Sun, W.; Yang, Y.; Chen, C.; Ni, J. *J. Colloid Interface Sci.* **2011**, *356*, 211–216.
(35) Pan, J.; Liu, G.; Lu, G. Q.; Cheng, H.-M. *Angew. Chem., Int. Ed.* **2011**, *50*, 2133–2137.
(36) Pan, J.; Wu, X.; Wang, L.; Liu, G.; Lu, G. Q.; Cheng, H. M. *Chem. Commun.* **2011**, *47*, 8361–8363.
(37) Jitputti, J.; Suzuki, Y.; Yoshikawa, S. *Catal. Commun.* **2008**, *9*, 1265–1271.
(38) Bavykin, D. V.; Friedrich, J. M.; Walsh, F. C. *Adv. Mater.* **2006**, *18*, 2807–2824.
(39) Wang, N.; Lin, H.; Li, J.; Yang, X.; Chi, B.; Lin, C. *J. Alloys Compd.* **2006**, *424*, 311–314.
(40) Zhang, M.; Jin, Z.; Zhang, J.; Guo, X.; Yang, J.; Li, W.; Wang, X.; Zhang, Z. *J. Mol. Catal. A* **2004**, *217*, 203–210.
(41) Xiao, N.; Li, Z.; Liu, J.; Gao, Y. *Thin Solid Films* **2010**, *519*, 541–548.
(42) Qi, F.; Moiseev, A.; Deubener, J.; Weber, A. *J. Nanopart. Res.* **2011**, *13*, 1325–1334.
(43) Yu, J. G.; Yu, H. G.; Cheng, B.; Zhao, X. J.; Yu, J. C.; Ho, W. K. *J. Phys. Chem. B* **2003**, *107*, 13871–13879.
(44) Kleinhammes, A.; Wagner, G. W.; Kulkarni, H.; Jia, Y.; Zhang, Q.; Qin, L. C.; Wu, Y. *Chem. Phys. Lett.* **2005**, *411*, 81–85.
(45) Teoh, W. Y.; Denny, F.; Amal, R.; Friedmann, D.; Mädler, L.; Pratsinis, S. E. *Top. Catal.* **2007**, *44*, 489–497.
(46) Franch, M. I.; Ayllón, J. A.; Peral, J.; Domènech, X. *Catal. Today* **2002**, *76*, 221–233.
(47) Weisz, A. D.; García Rodenas, L.; Morando, P. J.; Regazzoni, A. E.; Blesa, M. A. *Catal. Today* **2002**, *76*, 103–112.
(48) Tran, H.; Scott, J.; Chiang, K.; Amal, R. *J. Photochem. Photobiol., A* **2006**, *183*, 41–52.
(49) Ribbens, S.; Caretti, I.; Beyers, E.; Zamani, S.; Vinck, E.; Van Doorslaer, S.; Cool, P. *J. Phys. Chem. C* **2011**, *115*, 2302–2313.

(50) Li, W.; Bai, Y.; Liu, C.; Yang, Z.; Feng, X.; Lu, X.; Van Der Laak, N. K.; Chan, K. Y. *Environ. Sci. Technol.* **2009**, *43*, 5423–5428.
(51) Yang, D.; Liu, H.; Zheng, Z.; Yuan, Y.; Zhao, J. C.; Waclawik, E. R.; Ke, X.; Zhu, H. *J. Am. Chem. Soc.* **2009**, *131*, 17885–17893.
(52) Zhou, W.; Du, G.; Hu, P.; Li, G.; Wang, D.; Liu, H.; Wang, J.; Boughton, R. I.; Liu, D.; Jiang, H. *J. Mater. Chem.* **2011**, *21*, 7937–7945.
(53) Denny, F.; Scott, J.; Chiang, K.; Teoh, W. Y.; Amal, R. *J. Mol. Catal. A: Chem.* **2007**, *263*, 93–102.